J Solid State Electrochem (2012) 16:93–100
DOI 10.1007/s10008-010-1279-2

ORIGINAL PAPER

Electrochemical synthesis and nucleation and growth mechanism of Prussian blue films on p-Si(100) electrodes

Eduardo Carlo Muñoz · Ricardo A. Córdova · Rodrigo G. Henríquez · Ricardo S. Schrebler · Regina Cisternas · Ricardo E. Marotti

Received: 27 August 2010 / Revised: 8 December 2010 / Accepted: 9 December 2010 / Published online: 5 January 2011

Abstract In this study, we examined the synthesis of Prussian blue onto p-Si(100). The Prussian blue formation was carried out by means of the deposition of a Fe film and then its dissolution in presence of potassium hexacyanoferrate(II). In the first stage, a study by cyclic voltammetry was carried out, and then, using the potential step method, the corresponding nucleation and growth mechanism were determined. Likewise, a morphologic analysis of the deposits obtained at different potential values by means of atomic force microscopy was carried out. The results are consistent with a 3D progressive nucleation with diffusion-controlled growth. Finally, this research is oriented to construct electrochemical storage devices which can be in situ loaded by the photovoltaic action of the semiconductor base material doped silicon.

Keywords Prussian blue · P-silicon · Nucleation and growth · 3D progressive nucleation

E. C. Muñoz (✉) · R. A. Córdova · R. G. Henríquez · R. S. Schrebler · R. Cisternas
Instituto de Química, Facultad de Ciencias,
Pontificia Universidad Católica de Valparaíso,
Casilla 4059,
Valparaíso, Chile
e-mail: eduardo.munoz.c@ucv.cl

R. E. Marotti
Instituto de Física, Facultad de Ingeniería,
Universidad de La República,
Herrera y Reissig 565, C.C. 30,
11000 Montevideo, Uruguay

Introduction

Metal hexacyanometallates (MeHCM) are compounds that lend itself to a detailed study of the insertion electrochemistry. These correspond to mixed-valence compounds where Prussian Blue (PB) or iron (III) hexacyanoferrate(II) (with A=K and M=Z=Fe in the above generic formula) being the classical prototype. This type of compounds have been widely studied, therefore, the knowledge, related to structure [1–10], redox properties [11–15], applications [16–18], among others, is clearly described in the concerning literature. Nevertheless, in spite of the above, studies concerned with the nucleation and growth mechanism (NGM) of these compounds, deposited on electrode surfaces, have received scarce interest, with only a couple of researches existing on this theme [19, 20]. Research in this area is important because it would provide interesting information about how these phases are formed on a determined electrode substrate, especially if certain properties of these MeHCM compounds were found to be applicable to the modification of an electrode surface for a determined purpose. Similarly, according our knowledge, a study about the NGMs of cyanometallate compounds on a semiconductor surface, and specifically on silicon, has not been performed. As it is known, silicon is a semiconductor substance that has been broadly employed as a solar energy converter material in photovoltaic/photoelectrochemical cells as well as a photoelectrocatalyst material in reactions of technological and environmental interest [21–29]. Nevertheless, under determined conditions, silicon suffers photocorrosion which limits its applicability. Notwithstanding, the silicon photocorrosion could be avoided if a surface film of a compound like a MeHCM film could be formed on it. Thus,

the MeHCM surface film on silicon not only would limit or avoid the recombination electron/hole by means of the capture of the photogenerated holes, but also would control the moisture degree of the silicon surface [30, 31]. On the other hand, taking into account the semiconductor character of silicon and the wide range of redox potential that is present the family of MeHCM [32, 33], it is possible to imagine that an adequate coupling of silicon/MeHCM would be the base for the design of efficient photovoltaic systems for accumulating energy. In order to achieve this objective, the deposit of the MeHCM film on silicon must be thin, adherent, and optically transparent to the exciting photons. Therefore, a control of the characteristics of the deposit of MeHCM to be obtained on silicon must start, getting information on how this deposit takes place, and in this sense, a study about the NGM of these substances on a silicon substrate appear as very important.

In the present article, the NGM of a PB phase electroformed onto p-Si(100) was performed by the method of potentiostatic pulses. The PB phase was formed by the two-step electrosynthesis strategy. Firstly, a Fe film was previously electrodeposited onto a silicon substrate from an acidic Fe (III) ion solution. In the second step, the Fe film obtained, after transfer to an aqueous solution containing the potassium hexacyanoferrate (II) salt, was anodically stripped, and the PB phase formation takes place onto the silicon electrode. Thus, the control of the ionic product in the electrode–solution interface (which permits the control of the precipitation of PB) was possible by tuning the applied potential value. The current density/time transients, *i*/*t*, obtained under different potential conditions, were analyzed and interpreted according to the laws that govern the electrodeposits of the metallic phases on metallic electrode substrate.

Experimental section

Prussian blue deposition was performed on monocrystalline p-Si (100) with a resistivity between 0.01–0.3 Ωcm ($N_A \cong 5\times10^{17}$ cm^{-3}) B-doped and polished/etched surfaces (Int. Wafer Service, CA, USA). The silicon wafer was cut into rectangles (1.0×2.5 cm^2) that were first degreased in boiling acetone for 10 min. Then, they were sequentially cleaned ultrasonically for 10 min in acetone, ethanol, and finally with water. Next, the electrodes were treated for 10 min with a 1:1 H_2SO_4/H_2O_2 (98% *w*/*w* and 30% vol) mixture heated up to 80 °C in order to remove any trace of heavy metals and organic species. Afterwards, the oxide film was removed by etching with 4% hydrofluoric acid (HF) solution for 2 min and thoroughly rinsed with ultra pure water. The ohmic contact was made with InGa eutectic on the etched face of the samples, and the electrodes were mounted onto a Teflon holder. The silicon area exposed to the solution was 1.0 cm^2. Before the experiments, the electrode surface was again etched for 2 min in 4% HF solution. For each measurement, a new electrode of p-Si (100) was used, due to the well-known fact that some metals can diffuse into the inner of silicon [34, 35].

For the voltammetric studies of Prussian blue deposition, a platinum wire was used as a counter electrode, and mercury/mercury sulfate electrode (Hg/Hg_2SO_4, K_2SO_4 (saturated), 0.640 V vs. NHE) was used as a reference electrode. All the potentials reported in this study refer to this reference electrode.

The electrolytic solutions were prepared using distilled and deionized water (Millipore) with a resistivity of 18 MΩ cm. Analytical grade reagents from Merck (H_3BO_3, Na_2SO_4, K_2SO_4, $Fe_2SO_4{\cdot}7H_2O$, H_2SO_4) and Fluka ($K_4[Fe(CN)_6]\times3H_2O$) were used.

Two electrochemical cells were used in the experiments; both of them were made of Teflon and possessed an optical pass. Cell (1) was used for recording the voltamogramms and for the Fe deposition. The latter was achieved by means of chronoamperometry in a solution containing 0.02 M H_3BO_3+0.1 M Na_2SO_4+0.1 M K_2SO_4+0.02 M $Fe_2SO_4{\cdot}7H_2O$+0.01 M H_2SO_4. The oxidation of iron to Prussian blue was performed in cell (2) with a solution containing 0.02 M H_3BO_3+0.1 M Na_2SO_4+0.1 M K_2SO_4+0.02 M $K_4[Fe(CN)_6]\times3H_2O$+0.01 M H_2SO_4.

The following protocol was followed: following the cleaning procedure (see above), the p-Si(100) electrode was mounted in the Teflon holder leaving 1 cm^2 as the electrode surface area exposed to the solution. Then, the electrode was transferred to cell (1) where, in the first stage, the voltammetric characterization of iron deposition was carried out, and later, a new p-Si substrate was used for the potentiostatic iron deposition process which was followed by chronoamperometry, keeping the overall charge for deposition at 3 C. After this procedure, the electrode was washed and immersed in the solution containing the hexacyanoferrate (II) solution. Cyclic voltammetry experiments were carried out at room temperature and at a scan rate of 0.010 Vs^{-1}. All the measurements were carried out under illumination unless the opposite is indicated. Illumination was performed with a xenon lamp of 75 W (Oriel Instruments 6263) mounted in a lamp holder (Oriel 66902) and using a water filter (Oriel 61945) and a 1 m length optical fiber (Oriel 77578). A power supply of 40–200 W (Oriel 68907) was used to generate the arc in the lamp. The illumination power was quantified inside the cell by means of a power meter (Oriel 70260). The samples illuminated with the Xe lamp reach a light intensity of 4.0 mW cm^{-2}. A pure argon stream was passed through the solution for 30 min before measurements, and over the solution during the experiments.

The electrochemical measurements (cyclic voltammetry and chronopotentiometry) were performed using Princeton Applied Research model 273A equipment. All samples used for ex situ AFM were prepared in the electrochemical cell (1). The AFM images were obtained with a Digital Instrument Nanoscope IIIa series employed in tapping mode at a scan rate of 0.02 μm/s.

Results and discussion

Cyclic voltammetry analysis of iron deposition onto p-Si (100) under illumination

Figure 1 shows the potentiodynamic *j*/*E* profiles for a p-Si (100) electrode in 20 mM $FeSO_4 \times 7H_2O$+0.1 M Na_2SO_4+ 20 mM H_3BO_3+0.01 M H_2SO_4 solution under illumination. In this Figure, in the initial negative scan, a cathodic peak (1) starts at about −1.1 V which is attributed to the iron electrodeposition process and the hydrogen evolution reaction. In the positive scan, the current presents a hysteresis indicating the increase of the hydrogen evolution reaction on the growing iron layer. At −0.8 V, a cross-linking of the currents (forward and reverse scans) was observed, which can be associated to the reversible potential Fe^0/Fe^{2+}. At potentials more positive than −0.8 V, a peak is developed at −0.5 V associated to iron dissolution designed by number 2.

Taking a new p-Si(100) electrode, a potential of −1.3 V was imposed, and the iron deposition was followed by chronoamperometry. At this potential value, the iron electrodeposition takes place. The process was interrupted when the passed charge density was 3 $C cm^{-2}$. Considering a preferential crystalline plane of (111), the charge corresponding to 1 monolayer is $Q_{ml,111}=\frac{2ze\sqrt{3}}{3d^2}=\frac{4ze\sqrt{3}}{3a_0^2}$ where the iron atomic diameter, *d*, is 0.252 nm. Therefore, the equivalent charge to an iron monolayer is 0.579 mC cm^{-2}. Moreover, a charge value of 3 $C cm^{-2}$ corresponds to approximately 5,180 monolayers, corresponding to a thickness of 1.3 μm (assuming a 100% of faradaic yield). With these approximations and for a visual inspection, we assumed that the p-Si substrate was completely covered with an iron film. Later, the p-Si/Fe modified substrate was immersed in a 20 mM $K_4Fe(CN)_6$+0.1 M K_2SO_4+20 mM H_3BO_3+0.01 M H_2SO_4 solution, and the current density versus potential was recorded for an oxidation scan. This voltammogram is depicted in Fig. 2.

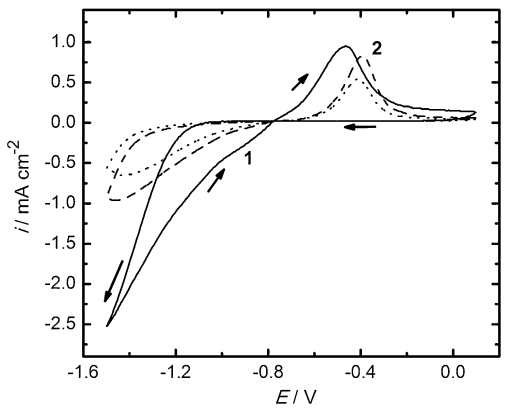

Fig. 1 Potentiodynamic *i*/*E* profiles of p-Si electrode in an iron(II) solution. First, fifth, and tenth cycles correspond to *solid*, *dash* and *dot lines*, respectively. The *direction of solid arrow* indicates the increase of the number of cycles

This voltammogram presents a complex process attributed to oxidation of iron film between −0.9 V and −0.3 V. In this, it is possible to observe a peak localized at −0.55 V, which would indicate the dissolution of iron film by holes in valence band of semiconductor, and then, the precipitation process of Prussian blue considering the following reaction.

$$Fe_{(s)} \rightarrow Fe^{3+}_{(aq)} + 3e^- \quad (1a)$$

$$Fe^{3+}_{(aq)} + \left[Fe^{II}(CN)_6\right]^{4-}_{(aq)} + K^+_{(aq)} \rightarrow K\left\{Fe^{III}\left[Fe^{II}(CN)_6\right]\right\}_{(s)} \quad (1b)$$

At potentials more positive than −0.3 V, silicon oxide formation is observed. Based on these observations, the p-Si/Fe modified electrode was polarized at −0.8 V for 100 s, with the aim to ensure a complete conversion of the metallic iron to PB, which was confirmed by direct observation.

Nucleation and growth mechanism: *j*/*t* transient analysis for p-Si/PB interface

Determination of the nucleation and growth mechanisms of PB on p-Si was carried out by means of the analysis of the

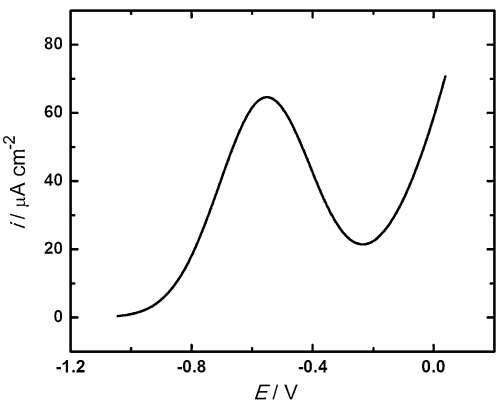

Fig. 2 Potentiodynamic *i*/*E* profile of p-Si/Fe electrode in a potassium hexacyaneferrate(II) solution

j/*t* transients. In Fig. 3a are shown the chronoamperometric transients at different potential values, obtained from the dissolution of four iron films under conditions mentioned above. This dissolution was carried out in the presence of potassium hexacyanoferrate(II) allowing a supersaturation of iron ions at the interface and thus the precipitation of PB

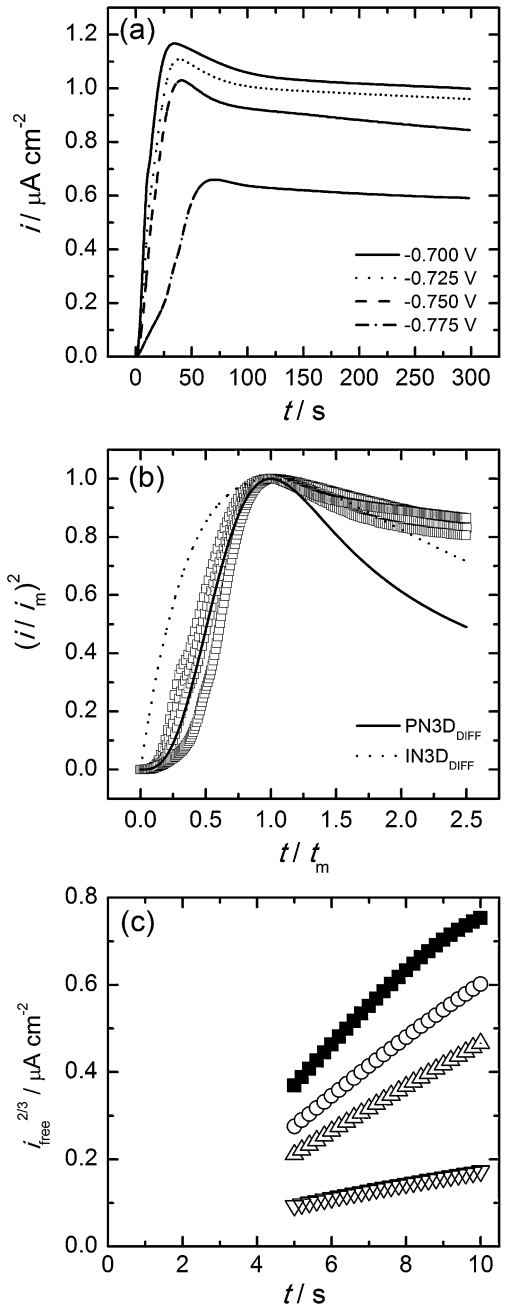

Fig. 3 *i*/*t* transients for iron dissolution and subsequent Prussian blue precipitation onto a p-Si(100) for potential steps indicated in the figure (**a**). In **b**, dimensionless plots for the current transients from (**a**), *solid* and *dot lines* correspond to the calculated curve for the growth laws for 3D diffusion-controlled instantaneous and progressive nucleation mechanisms, respectively. In **c**, $i_{free}^{2/3}$ vs. *t* plot for the transients from (**a**) before the current and time maximum: *inverted triangle* −0.775 V, *triangle* −0.750 V, *white circle* −0.725 V, *black square* −0.700 V

according to the applied potential. The transients are characterized by an initial increase in the current value and then a decay that reaches a constant value at longer times (>100 s). This initial increase in the current is due to the iron dissolution and subsequent nucleation and growth of PB onto silicon. Then, these growth centers, together with their respective diffusion zones, begin to overlap inducing a decrease in the deposition area, and this way, a decrease in the current density value until a limit is reached. Another important aspect is that when the potential value is more positive, the time (t_{max}) corresponding to the current maximum (i_{max}) decreases and the current maximum value increases. These aspects could be associated with a nucleation of hemispherical centers under diffusion-controlled growth. However, it must be considered that the position of the current maximum can be associated to mixed control regimes: complete charge transfer and combined charge transfer and diffusion control which correspond to the limitations of the growth kinetics. Furthermore, the shift of t_{max} and i_{max} can be considered valid not only for hemispherical clusters but also for different geometrical forms. As a first criterion and in order to determine the nucleation and growth mechanisms of PB on p-Si (100), we tried to distinguish between instantaneous and progressive nucleation; the experimental data are represented in a nondimensional form. Figure 3b gives the data from Fig. 3a in coordinates $(i/i_{max})^2$ versus t/t_{max}. This is in accordance with the theoretical models of nucleation and diffusion-controlled growth of hemispherical clusters. The models for instantaneous and progressive nucleation are given by Eqs. (2a) and (2b), respectively [36, 37]:

$$\frac{i^2}{i_{max}^2} = 1.9542 \cdot \left(\frac{t_{max}}{t}\right) \cdot \left[1 - \exp\left(-1.2564 \frac{t}{t_{max}}\right)\right]^2 \quad (2a)$$

$$\frac{i^2}{i_{max}^2} = 1.2254 \cdot \left(\frac{t_{max}}{t}\right) \cdot \left[1 - \exp\left(-2.3367 \frac{t^2}{t_{max}^2}\right)\right]^2 \quad (2b)$$

where i_{max} is the current and t_{max} is the time coordinate of a chroamperometric peak. As can be seen from Fig. 3b in the initial portion, the experimental data follow a three-dimensional progressive nucleation with diffusion-controlled growth mechanism, $i(t)_{PN3D_{diff}}$. However, after t_{max}, large deviations in this model can be observed. These deviations can be attributed to the presence of a parallel reaction to the PB electroprecipitation, attributed to the silicon oxide formation, $i(t)_{PR}$. Moreover, when only the initial part of the *i*/*t* transients (before maximum) is considered, a i_{free} vs. *t* plot is obtained. This is in order to exclude overlapping effects of growing 3D PB clusters and/or diffusions zones. Figure 3c shows the initial parts of the transients in a $(i_{free})^{2/3}$ versus *t* plot. The obtained linear relationship corresponds to a nucleation and growth model including progressive

nucleation which confirms the model deduced from nondimensional plots. Finally, i_{free} is given by [38, 39]:

$$i_{free}^{2/3} = -nF\frac{2}{3}\pi \cdot V_m^{1/2} \cdot k_n N_0 \cdot (2 \cdot D \cdot C^{\infty})^{3/2} \cdot \left[1 - \exp\left(\frac{nF|\eta|}{RT}\right)\right]^{3/2} (t - t_o) \quad (3)$$

Where $n{\cdot}F$ is the molar charge transferred during the process, D, C^{∞}, and V_m are the diffusion coefficient, the concentration in the bulk of solution, and the molar volume of the iron hexacyaneferrate species, respectively. k_n and N_0 are the steady state nucleation rate constant per nucleation site (for first order) and surface active sites density, respectively. The product between both parameters is the nucleation rate.

In accordance with the above, the experimental i/t transients were then fitted using a mathematical function sum of the two contributions. The best results were found with the Eq. 4:

$$i(t)_{total} = \underbrace{P_{(1)}t^{-1/2}\cdot[1 - \exp(-P_{(2)}t^2)]}_{i(t)_{PN3D_{diff}}} + \underbrace{P_{(3)}\cdot[1 - \exp(-P_{(4)}t^3)]}_{i(t)_{PR}} \quad (4)$$

Where $P_{(1)} = \frac{nFD^{\frac{1}{2}}C^{\infty}}{\sqrt{\pi}}$, $P_{(2)} = \frac{4}{3}k_n N_0 \pi^{\frac{3}{2}} D\left(\frac{8C^{\infty}M}{\rho}\right)^{\frac{1}{2}}$, $P_{(3)} = nFk_{SiO_2}$, and $P_{(4)} = \frac{\pi M^2 k_{SiO_2}^2 k_n N_0}{3\rho^2}$. n F is the molar charge transferred during the process; D, C^{∞}, M and ρ are the diffusion coefficient, the concentration in the bulk solution, the molar mass, and the density of the iron species, respectively; $k_n N_0$ is the nucleation rate; k_{SiO2} is the constant rate during the silicon oxide formation.

Figure 4 shows the experimental and fitted (with the global eq. 4) i/t transients recorded at different potential values. The fitted error range was 0.1−2%. The separated contributions for each term are also shown in Fig. 4, and the electric charge associated with each contribution expressed as percentages of the transient total charge is summarized in Table 1.

On the basis of the results shown in Fig. 4 and the values presented in Table 1, it can be concluded that the parallel reaction (PR) is the most important contribution. This is an indication that the PB electroprecipitation process on p-Si(100) is not the main one. In fact, the parallel contribution appears in an appreciable form at $t > t_{max}$, which indicates that this contribution is responsible for the misfit that appears in the nondimensional plot. According to the results obtained by means of the progressive nucleation followed by three-dimensional diffusion-limited growth in equation 4, t_{max} and i_{max} are given by [34, 36, 37]:

$$i_{max} = 0.4959 \cdot n \cdot F \cdot D^{\frac{3}{4}} \cdot C^{\infty\frac{9}{8}} \cdot (8 \cdot \pi \cdot V_m)^{\frac{1}{8}} \cdot (k_n N_0)^{\frac{1}{4}} \quad (5a)$$

$$t_{max} = 3.31 \cdot D^{-\frac{1}{2}} \cdot (8 \cdot \pi \cdot C^{\infty} \cdot V_m)^{-\frac{1}{4}} \cdot (k_n N_0)^{-\frac{1}{2}} \quad (5b)$$

Assuming that the nucleation rate, $k_n N_0$, is the only potential-dependent term in the expressions for i_{max} and

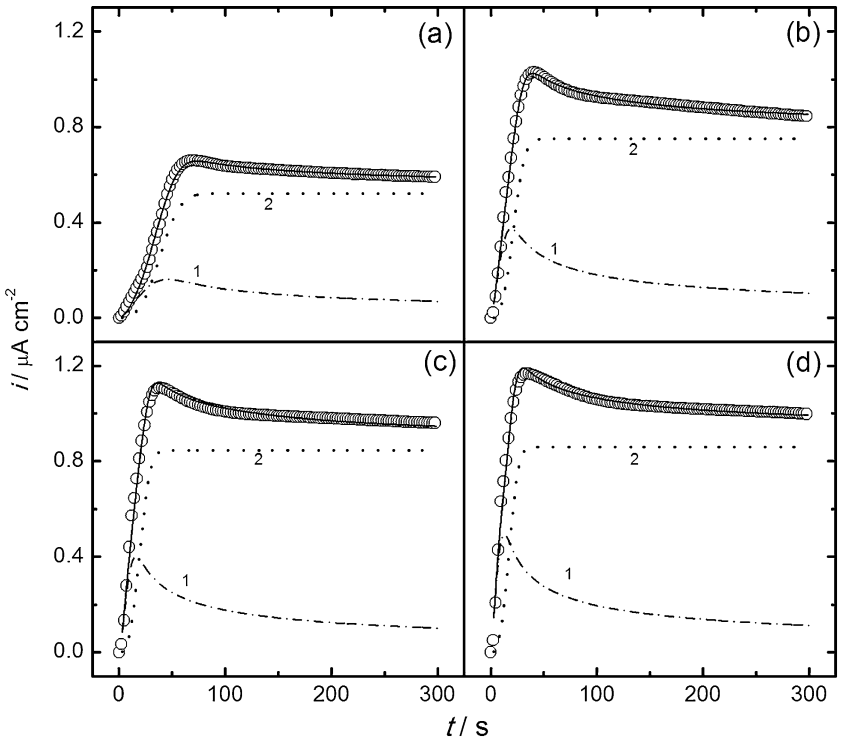

Fig. 4 Experimental (*white circle*) and theoretical (*solid line*) i/t transients after non-linear fitting of Eq. 4. At a deposition potential: **a** −0.775 V, **b** −0.750 V, **c** −0.725 V and **d** −0.700 V. *Dashed lines* (*1*) correspond to the $PN3D_{Diff}$. *Dotted lines* (*2*) correspond to the PR contributions

Table 1 Electric charge and percentage of the total charge associated with the contributions $PN3D_{Diff}$ and PR obtained from the *i*/*t* transients in Fig. 5 fitted with Eq. 4

E/V	Exp. total charge (μC cm^{-2})	Calc. total charge (μC cm^{-2})	$i(t)_{PN3D_{diff}}$ charge (%)	$i(t)_{PR}$ charge (%)
−0.775	165	165.2	17.7	82.2
−0.750	258.4	259.8	19.7	80.3
−0.725	286.9	289.7	18.2	81.7
−0.700	303	300.2	19.1	80.8

t_{max}, deriving regarding to potential and combining both equations, we obtain:

$$\frac{dE}{d\log i_{max}} = -2\frac{dE}{d\log t_{max}} \quad (6)$$

Figure 5a shows the dependence of log t_{max} and log i_{max} with the potential. Considering the slope values of these relations, $dE/d(\log t_{max}) = -128\text{mV/dec}$ and $dE/d(\log i_{max}) = 256.4\text{mV/dec}$, the $d(\log t_{max})/d(\log i_{max})$ coefficient was determined. This value corresponds to −1.97 corroborating the model. The nucleation rate k_nN_0 can be obtained by combining the equations for i_{max} and t_{max} where we obtain [36, 37]:

$$J_{nucl} = k_nN_0 = 0.2898 \times (8\pi C^{\infty}V_m)^{-\frac{1}{2}}\frac{(nFC^{\infty})^2}{i_{max}^2 t_{max}^3} \quad (7)$$

Additionally, the rate of nucleation can be represented by the classic Volmer–Weber equation [40]:

$$J_{Nucl} = A_{3D}\exp\left(-\frac{\Delta G_{crit}}{kT}\right) \quad (8)$$

Where the pre-exponential factor A_{3D} is only weakly dependent on the overpotential, and the critical energy for growth of a nucleus is given by [41]: $\Delta G_{crit} = 4B \cdot V_m^2 \cdot \sigma^3/27(e|\eta|)^2$ Where B is a geometrical factor (36π for a sphere, 6^3 for a cube), V_m is the atomic volume and σ is the average surface energy. Considering the definition related to the overpotential dependence of the critical cluster size [41] as: $N_{crit} = 8B \cdot V_m^2 \cdot \sigma^3/27(e|\eta|)^3$and combining the eq. 8 with the last two equations defined in the before paragraph, we obtain:

$$\frac{d\log J_{Nucl}}{d|\eta|} = -\frac{1}{kT}\frac{d\Delta G_{crit}}{d|\eta|} = \frac{e}{2.303kT}N_{crit} \quad (9)$$

Hence, by plotting log (k_nN_0) versus the overpotential, the number of atoms required to form the critical nucleus size can be obtained from the slope. Figure 5b shows log (k_nN_0) vs. potential for the system examined in this study, and it indicates that the nucleation rate increases exponentially with the applied potential. The N_{crit} value found from the slope value of the plot shown in Fig. 6b was <1. The N_{crit} <1 result is not a rare event when electrochemical nucleation takes place on a foreign substrate. According to Milchev et al. [42], a critical nucleus consisting of zero particles can be obtained when the nucleation proceeds on active centers. In this case, at sufficiently high supersaturation, applying a positive overpotential, the iron(III) concentration at the interface reaches the ionic product of Prussian blue. An active center on silicon can be considered as a stable center for growth, playing the role of a critical nucleus. Furthermore, according to Gunawardena et al. [43], the significance of small values of N_{crit} is hard to evaluate, and they may simply be the result of the application of a high overpotential, as it was observed by these authors. Therefore, the determination of N_{crit} by

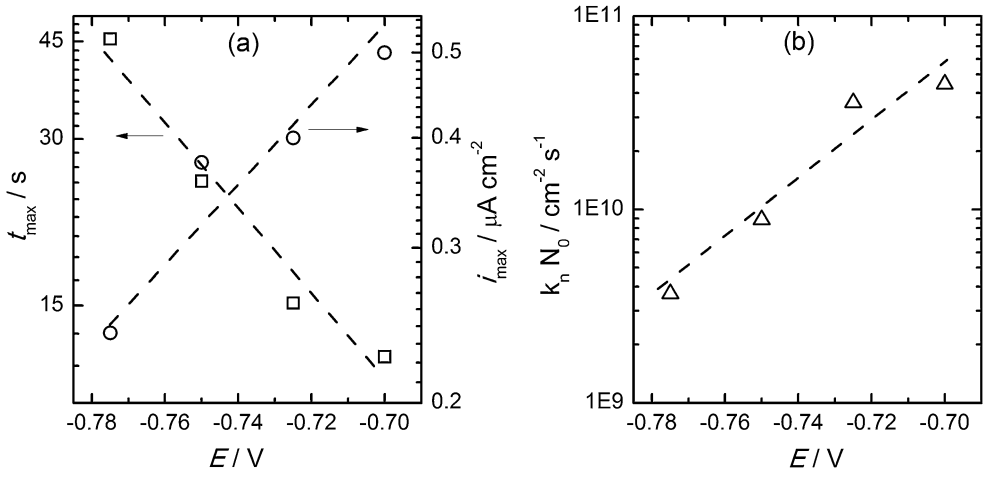

Fig. 5 **a** Semilogarithmic plot of the t_{max} and i_{max} as a function of the potential. **b** Semilogarithmic plot of the nucleation rate calculated from eq. 7 as a function of the potential

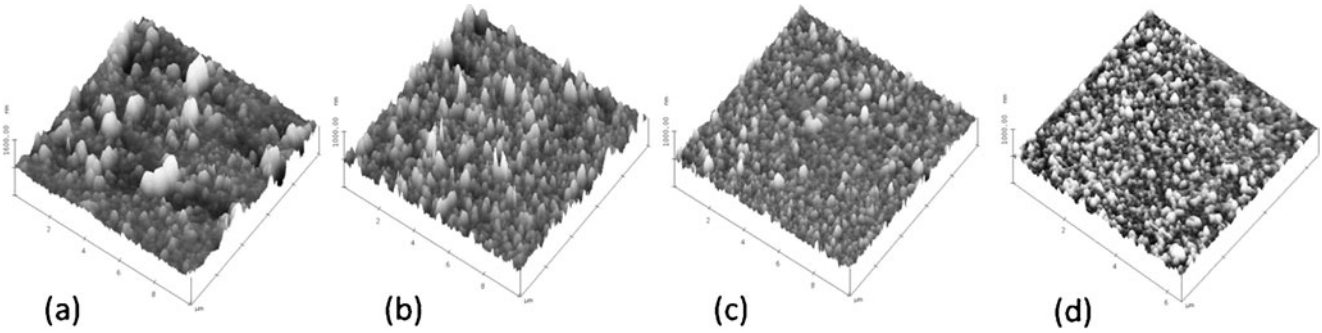

Fig. 6 3D AFM images of Prussian blue particles on p-Si(100) deposited at different potential values until reaching a constant charge value of 3.0 mC cm^{-2}. **a** −0.775 V, **b** −0.750 V, **c** −0.725 V, **d** −0.700 V

means of this classical approach constitutes an approximation and must be considered a different type of experimentation in the future.

Morphology of Prussian blue deposits as studied by atomic force microscopy

As discussed above, from the *j*/*t* transient analysis, a 3D progressive nucleation and growth mechanism has been derived, and this should be reflected in the morphology of the films. To corroborate this, a study of the morphology of the films was carried out by AFM in tapping mode technique. Figure 6 shows 8×8-μm AFM images of Prussian blue films deposited onto p-Si(100) at different potential values under illumination. The iron electrodissolution and the subsequent PB precipitation process was stopped after a constant charge value of 3.0 mC cm^{-2}, which is equivalent to about 5–6 monolayers. This last value was calculated considering that the charge of the iron dissolved monolayer is 0.576 mC cm^{-2} for the (111) plane. In fact, the XRD measurements (not included) indicate a preferential plane (111) for the iron deposit on p-Si(100).

Indeed, 3D particle (nuclei) growth can be seen in the AFM images. The particle density increased when the potential was more positive. Given that the charge for deposition was always constant, the particle density increased, and then their size decreased. All these are in line with progressive nucleation and 3D growth in the island mode mechanism (Volmer–Weber mechanism) [34, 44–47].

Conclusions

The study of Prussian blue synthesis by means of precipitation on p-Si(100) indicates that the nucleation and growth mechanism corresponds to a 3D progressive nucleation and diffusion-limited growth ($PN3D_{Diff}$), mechanism confirmed by means of AFM. However, it is important to notice that the presence of a parallel redox reaction to the electroprecipitation process produces deviations from the nucleation and growth models when they are fitted to experimental data. In this context, an expression for this parallel reaction corresponding to the silicon oxide formation was proposed. Finally, it was demonstrated that the Prussian blue formation onto p-Si(100) is possible. In future researches, we will show the photoelectrochemical and optical characterization of this film onto silicon.

Acknowledgment We thank FONDECYT, Chile for the financial support for this study (grant no. 1090217) and the Dirección de Investigación e Innovación of the Pontificia Universidad Católica de Valparaíso (grant no. 037.108/2008 DII-PUCV). E. Muñoz and R. Henríquez thank Programa Bicentenario de Ciencia y Tecnología, PSD82. R. E. Marotti also acknowledges the support received from CNPq (Brazil, Prosul Program, Project # 490580/2008-4), PEDECIBA–Física, Administración Nacional de Investigación e Innovación (ANII) and the Comisión Sectorial de Investigación Científica (CSIC) of the Universidad de la República, in Montevideo, Uruguay. Special thanks to Fritz Scholz of the Ernst-Moritz-Arndt-Universität Greifswald for his collaboration on the discussion of this work.

References

1. Buser HJ, Schwarzenbach D, Petter W, Ludi A (1977) Inorg Chem 16:2704–2710
2. Song YY, Jia WZ, Li Y, Xia XH, Wang QJ, Zhao JW, Yan YD (2007) Adv Func Mater 17:2808–2814
3. Tsiafoulis CG, Trikalitis PN, Prodromidis MI (2005) Electrochem Commun 7:1398–1404
4. Yang J, Wang H, Lu L, Shi W, Zhang H (2006) Crys Growth Des 6:2438–2440
5. Valsala TP, Joseph A, Shah JG, Kanwar R, Venugopal V (2009) J Nucl Mater 384:146–152
6. Zhao J, Zhang Y, Shi C, Chen H, Tong L, Zhu T, Liu Z (2006) Thin Solid Films 515:1847–1850
7. Vo V, Van MN, Lee HI, Kim JM, Kim Y, Kim SJ (2008) Mater Chem Phys 107:6–8
8. Agnihotry SA, Singh P, Joshi AG, Singh DP, Sood KN, Shivaprasad SM (2006) Electrochim Acta 51:4291–4301

9. Zhou P, Xue D, Luo H, Chen X (2002) Nano Lett 2:845–847
10. Choudhury S, Dey GK, Yakhmic JV (2003) J Cryst Growth 258:197–203
11. Sabzi RE, Hasanzadeh A, Ghasemlu K, Heravi P (2007) J Serb Chem Soc 72:993–1002
12. Chen SM, Chan CM (2003) J Electroanal Chem 543:161–173
13. Orellana M, Arriola P, del Río R, Schrebler R, Cordova R, Scholz F, Kahlert H (2005) J Phys Chem B 109:15483–15488
14. Ellis D, Eckhoff M, Neff VD (1981) J Phys Chem 85:1225–1231
15. Schröder U, Scholz F (2000) Inorg Chem 39:1006–1015
16. Zhao H, Yuan Y, Adeloju S, Wallace GG (2002) Anal Chim Acta 472:113–121
17. Orellana M, Ballesteros L, Del Río M, Grez P, Schrebler R, Córdova R (2009) J Solid State Electrochem 13:1303–1308
18. Narayanan SS, Scholz F (1999) Electroanal 11:465–469
19. Orellana M, Del Río R, Schrebler R, Cordova R (2007) J Phys Chem C 111:17541–17550
20. Kuhnhardt C (1994) J Electroanal Chem 369:71–78
21. Nakato Y, Ueda K, Tsobomura H (1986) J Phys Chem 90:5495–5496
22. Szklarczk M, Bockris JO (1984) J Phys Chem 88:1808–1815
23. Dominey R, Lewis N, Bruce J, Bookinder D, Wrighton M (1982) J Am Chem Soc 104:467–482
24. Nakato Y, Tsobomura H (1992) Electrochim Acta 37:897–907
25. Nakato Y, Ueda K, Yano H, Tsobomura H (1988) J Phys Chem 92:2316–2324
26. Kubo N, Homma T, Hondo Y, Osaka T (2005) Electrochim Acta 51:834–837
27. Kuznetsov G, Skyryshevsy V, Vdovenkova T, Tsyganova A, Gorostiza P, Sanz F (2001) J Electrochem Soc 148:C528–C532
28. Harris L, Hugo J (1981) J Electrochem Soc 128:1203–1211
29. Gorostiza P, Díaz R, Sanz F, Morante JR (1997) J Electrochem Soc 144:4119–4122
30. Schrebler R, Muñoz E, Cury P, Suárez C, Gómez H, Córdova R, Dalchiele E, Marotti R (2006) J Phys Chem B 110:21109–21117
31. Muñoz EC, Schrebler RS, Córdova RA, Marotti RE, Dalchiele EA (2007) J Phys Chem B 111:16505–16515
32. Soto MB, Scholz F (2002) J Electroanal Chem 521:183–189
33. Rosseinsky DR, Glasser L, Brooke HD (2004) J Am Chem Soc 126:10472–10477
34. Oskam G, Vereecken PM, Searson PC (1999) J Electrochem Soc 146:1436–1441
35. Istratov AA, Weber ER (2002) J Electrochem Soc 149:G21–G30
36. Scharifker B, Hills G (1983) Electrochim Acta 28:879–889
37. Gunawardena G, Hills G, Montenegro I, Scharifker B (1982) J Electroanal Chem 138:225–239
38. Rashkova B, Gruel B, Pötzschke RT, Staikov G, Lorenz WJ (1998) Electrochim Acta 43:3021–3028
39. Ehlers C, König U, Staikov G, Schultze JW (2001) Electrochim Acta 47:379–385
40. Oskam G, Long JG, Natarajan A, Searson PC (1998) J Phys D Appl Phys 31:1927–1949
41. Budevski E, Staikov G, Lorenz W (1996) Electrochemical phase formation and growth. VCH, Weinheim
42. Milchev A, Stoyanov S (1976) J Electroanal Chem 72:33–43
43. Gunawardena G, Hills G, Montenegro I, Scharifker B (1982) J Electroanal Chem 138:241–254
44. Ji C, Oskam G, Searson PC (2001) J Electrochem Soc 148:C746–C752
45. Ziegler JC, Rietzle A, Bunk O, Zegenhagen J, Kolb DM (2000) Electrochim Acta 45:4599–4605
46. Oskam G, Searson PC (2000) J Electrochem Soc 147:2199–2205
47. Pötzschke RT, Staikov G, Lorenz WJ, Wiesbeck W (1999) J Electrochem Soc 146:141–149